A numerical study of the effects of cathode geometry on tungsten inert gas type electric arcs

Christopher Nahed, Stéphane Gounand, Marc Medale

Manuscript accepted in the *International Journal of Heat and Mass Transfer*, 2021. Preprint version.

A numerical study of the effects of cathode geometry on Tungsten Inert Gas type electric arcs

Christopher Nahed[1,2], Stéphane Gounand[1] and Marc Medale[2]

[1]DES-SEMT, CEA, Université Paris-Saclay, F-91191, Gif-sur-Yvette, France

[2]Aix-Marseille Université, CNRS, IUSTI, UMR 7343, F-13453, Marseille, France

Mailing address of the corresponding author: christopher.nahed@cea.fr

Short title for running head: *Effect of cathode geometry on TIG arcs*

Abstract

In this paper we address the question of the influence of cathode tip geometry on the physical quantities relevant to Tungsten Inert Gas (TIG) arc welding. Although cathode geometry is known to influence arc-plasmas, a thorough quantification of the Lorentz phenomenon, which is the dominant source of momentum in the fluid flow of TIG arcs has not been strongly investigated. Therefore, we have performed a numerical parametric study at a constant inlet electric current and arc height, for different cathode sizes and shapes (pointed, chamfered and rounded tips), parameterised by the truncation angle and tip radius. To this end, we developed a coupled steady-state magneto-hydrodynamic finite element model in a 2D axi-symmetric configuration, implemented in the CastɜM toolbox. The paper characterises, quantifies and analyses the influence of tip geometry on TIG arcs and the workpiece. The model reveals that tip size and truncation angle similarly influence the magnitude of the transported quantities of the arcs. We find that the imparted momentum and transferred heat flux to the workpiece vary about 4 and 2-fold between the bluntest and sharpest cathodes, respectively. This signifies the importance of the choice of cathode tips in numerical TIG welding simulations. Agreement between the literature and the current work is analysed and discussed and the importance of coupling the cathode and arc domains is highlighted.

Keywords: TIG Spot welding, electric arc, magneto-hydrodynamic flow, cathode tip geometry, parametric study.

Nomenclature

Symbol	Definition	SI Unit
α	truncation angle	degrees
β	edge angle	degrees
r_{int}	truncation radius	m
h	height	m
Ω	volume domain	m^3
Γ	domain interface	m^2
δl	length of modified conductivity	m
σ^*	electric conductivity	$\mathrm{S}\cdot\ \mathrm{m}^{-1}$
ϕ	electric potential	V
$\boldsymbol{B}$	magnetic flux density	T
μ_0	magnetic permeability	$\mathrm{A}\cdot\mathrm{m}^{-2}$
$\boldsymbol{j}$	electric current density	$\mathrm{A}\cdot\mathrm{m}^{-2}$
ρ	density	$\mathrm{kg}\cdot\mathrm{m}^{-3}$
μ	dynamic viscosity	$\mathrm{kg}\cdot\mathrm{m}^{-1}\cdot\mathrm{s}^{-1}$
$\boldsymbol{u}$	fluid flow velocity	$\mathrm{m}\cdot\mathrm{s}^{-1}$
P	fluid pressure	Pa
$\mathbb{I}$	identity tensor	
$\boldsymbol{f}_{\mathrm{Lor}}$	Lorentz force	$\mathrm{N}\cdot\mathrm{m}^{-3}$
τ	viscous shear stress	Pa
F	integrated force	N
λ	thermal conductivity	$\mathrm{W}\cdot\mathrm{m}^{-1}\cdot\mathrm{K}^{-1}$
T	temperature field	K
$\mathrm{s}_{\Omega,\Gamma}$	volume or surface heat source	$\mathrm{W}\cdot\mathrm{m}^{-[L]}$
c_p	specific heat	$\mathrm{J}\cdot\mathrm{kg}^{-1}\cdot\mathrm{K}^{-1}$
ϵ_n	plasma emissivity	$\mathrm{W}\cdot\mathrm{m}^{-3}$
ϵ	emissivity coefficient	
q	heat flux density	$\mathrm{W}\cdot\mathrm{m}^{-2}$
Q	integrated heat flux	W
σ_{B}	Stefan-Boltzmann constant	$\mathrm{W}\cdot\mathrm{m}^{-2}\cdot\mathrm{K}^{-4}$
$\boldsymbol{n}$	unit normal vector	
W	work function	V
k_B	Bolzmann constant	$\mathrm{J}\cdot\mathrm{m}^{-1}$
V_i	ionization potential	V
I_{imp}	total imposed electric current	A
$\boldsymbol{\sigma}$	stress tensor	Pa
$\mathcal{M}$	mesh	
n	number of iterations	
ε	minimum increment	K or $\mathrm{m}\cdot\mathrm{s}^{-1}$
$f_{\mathcal{M}}$	arbitrary function for given mesh	
Pe	Peclet number	
α_d	thermal diffusivity	$\mathrm{m}^2\cdot\mathrm{s}^{-1}$
L_{arc}	characteristic arc length	m
g	Gaussian function	
σ_g	Gaussian width	m
w	Weibull function	
λ_w	Weibull scale	m
k	Weibull shape	
$\mathcal{P}$	integrated power	W
η	process efficiency	

Abbreviations

TIG	Tungsten Inert Gas
PNT	pointed
CHF	chamfered
RND	rounded
CPI	cathode-plasma interface
API	anode-plasma interface
LDUt	lower diagonal upper threshold

1 Introduction

Tungsten inert gas (TIG) arc welding is a widespread technique used to join metallic pieces together. Direct current (DC) arcs are used to generate heat at high temperatures, allowing for the melting of the welding zone of the workpiece. The numerical modelling of such arcs has been of interest in recent years due to increasing computational power [25]. The study and modelling of TIG DC arcs is important as it allows the researcher to better understand the dynamic and thermal effects of the arc onto the weld pool of the workpiece. This motivates the nonlinear magneto-hydrodynamic finite element model used in this work, as adapted from Brochard's work [4]. A welding engineer is typically interested in the effectiveness of the cathode and arc at transporting heat to the work-piece. The arc stress forces on the anode are also of interest, because they can dynamically force the shape of the weld pool [26, 34]. The interaction of the arc and the weld pool is out of the scope of this work; however we present the interaction between the arc and the solid work piece. As arcs are powered by electric currents, a change in the input current density affects the arc behavior. Current density manifests through the emission zones (spots) of the cathode of an arc [1], therefore a change in spot area becomes a change in current density. The electron emission zone at a cathode can be the most influential boundary condition as it is the source of momentum for the arc [13, 8]. A TIG arc is thus sensitive to the variations in cathode shape [7]. The sensitivity of these arcs to cathode truncation angle has been studied both experimentally and numerically by multiple authors [11, 12, 29, 23, 27, 24]. Moreover, disagreement between numerical and experimental results (see Lago, Goodarzi, Tsai, Sadek [21, 11, 35, 29]) motivate a more careful analysis of the effect of cathode geometry onto TIG arcs. For example, Tsai [35] shows, experimentally, that convective heat transfer to the work piece increases as cathode truncation angle decreases, and that is not evident in the numerical results of Goodarzi [11]. Furthermore, not many numerical investigations into the effect of cathode tip size and shape, which can have strong effects on the arc [29], have been performed, as authors generally choose arbitrary pointed and chamfered tip shapes (see [11, 3]); thus motivating this work.

The plasmas of TIG arcs are hypothesized to be at local thermodynamic equilibrium (LTE), however their colder edges (particularly the electrode boundaries) deviate from LTE [10]. Moreover, due to the complexity of emission phenomena at cathode-plasma and anode-plasma interfaces (CPI, API), different approaches have been used when approximating current transport across or from the CPI. Authors like Hsu, Goodarzi, Alvarez impose cathode spots as boundary conditions (without incorporating a cathode into the computational domain), using experimentally estimated current densities [13, 11, 8]. Others use multi-species, non-LTE models to calculate current densities being emitted at the CPI [22, 30]. However, if computational simplicity is warranted, modelling the electrode sheaths, at the CPI and API, using equivalent source terms is possible. This 'LTE diffusion approximation' method [22] requires that the electrode sheaths have plasma-equivalent conductivities as calculated just outside the sheath zones.

This paper presents a parametric study, varying the the cathode tip geometry, the truncation angle and radius, quantifying the impact of cathode tips on the interaction of the arc with the workpiece. It aims to underline the influence of cathode geometry onto the "global welding performance", that highlights the induced magnetic pinching effects. The physical model used in the present work is based on the TIG arc model from Brochard [4], supplemented with the 'LTE diffusion approximation' method [22].

The parametric study underlines the importance of considering the cathode in the computational domain to reliably account for the magnetic pinching induced by the tip of the cathode. A characterisation, quantification and analysis of the influence of tip geometry on TIG arcs and the workpiece is undertaken. This reveals that tip size and truncation angle similarly influence the magnitude of the transported quantities of the arcs. Moreover, the imparted momentum and transferred heat flux to the workpiece vary about 4 and 2-fold between the bluntest and sharpest cathodes, respectively. Agreement between the literature and the current work is analysed and discussed and the importance of coupling the cathode and arc domains is highlighted.

The paper begins by presenting the geometric model and its parameterisation in section 2, then the governing

equations in section 3 along with the algorithm and the meshes used in section 4 and finally the results and conclusions in sections 5 and 6.

2 Geometric model

In this section, the problem geometry for a TIG spot configuration and its parameterisation is presented, assuming a rotational symmetry, as sketched in figure 1. The model accounts for a cathode, arc plasma and anode, in which both electrodes are assumed to remain in their solid state to highlight the behaviour of the arc plasma as a function of only the cathode geometry. The arc height is set to a constant value of 10 mm throughout the study. The parametric study is concerned with the effect of the variation of the cathode geometry at its tip. The considered shapes are a pointed cathode (PNT), a chamfered one (CHF) and a rounded (RND) one. The cathode is modelled as a solid thoriated tungsten (2% Th), the arc as an argon plasma and finally the anode as a solid copper piece. The geometry of the cathode is parameterised between the segments [AZ], [ZG], [GF], with a tip truncation angle α and a radius r_{int} at the tip. The range of the parameters are: $\alpha = [15^o,\ 20^o,\ 25^o\ , 30^o]$ and $r_{int} = [0.15$ mm, 0.3 mm, 0.6 mm]. Figure 1, b) presents a superimposition of the three considered cathode shapes. The axis of symmetry in figure 1 a) and b) is indicated by the dashed lines with dots.

The parameterisation of the geometry yields a total of 28 cases for the present parametric study. The widths and heights of the computational subdomains Ω_{cat}, Ω_{pla} and Ω_{ano} are kept constant throughout the study. The geometric parameters of the cathode are presented as follows (cf. figure 1):

$$h_{cat1} + h_{cat2} = 10 \text{ mm} \quad r_{int} = [0.15 \text{ mm},\ 0.3 \text{ mm},\ 0.6 \text{ mm}] \quad \alpha = [15^o,\ 20^o,\ 25^o,\ 30^o] \quad \beta = 90 - \alpha$$

$$h_{cat1} = \frac{2 - r_{int}}{\tan\alpha} \quad (1) \qquad r_{int,rnd} = \frac{r_{int}}{\tan(\beta/2)} \quad (2) \qquad r_{int,chf} = r_{int} \quad (3)$$

for all cases — rounded case — chamfered case

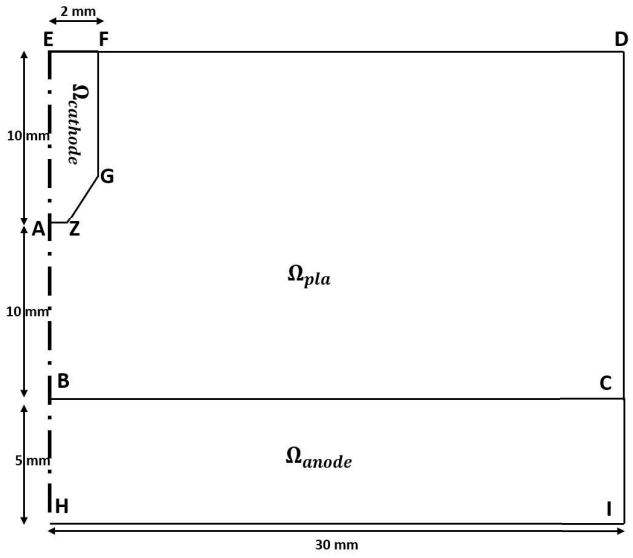

(a)

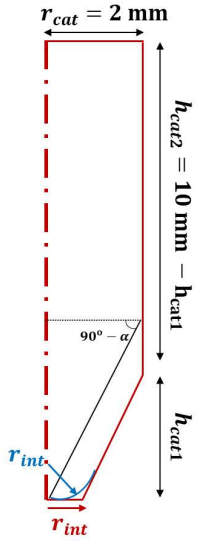

(b)

Figure 1: Sketches of the geometric parametric study. a) The computational domain. b) A close-up view of the three considered cathode shapes, superimposed.

3 Governing equations

This section presents the equations of our model as well as their respective boundary conditions. The temperature dependent physical properties of the cathode, plasma and anode are also presented. The model accounts for heat transfer, electromagnetic and hydrodynamic phenomena, under LTE assumptions, in the whole domain $\Omega_{tot} = \Omega_{cat} \cup \Omega_{pla} \cup \Omega_{ano}$. The fluid flow in the arc plasma is assumed to be laminar and couples the electric and magnetostatic equations to the hydrodynamic and heat transfer equations at steady state, as done by Brochard [4]. The volumic radiative energy loss in the arc is accounted for by using experimental emission values, following the work of Lago et al. [21].

The arc height of the configuration has been chosen such that the electrical effects at the plasma-anode interface become invariant with respect to the studied cathode geometries. This is due to the high electrical resistance of the 10 mm arc and this is discussed in subsection 5.2.1. Concerning the anode, a simple, purely conductive model has been considered for the purpose of performing numerous parametric studies at affordable computational cost. Furthermore, the high thermal and electrical conductivies of copper ensure that for a low anode thickness, the diffusive behaviour of both the thermal and electrical fields is significant [2, 15]. After preliminary testing, a thickness of 5 mm for the related anode thermo-electric model is chosen because it ensures the strong diffusivity of the solid copper anode.

3.1 Electromagnetic model

3.1.1 The electrode sheaths

The modelling of the electrode sheaths at the CPI and API would require non-LTE phenomena to differentiate between ionic and electronic transfers [22]. However, following the approach developed by Lowke et al. [22] one can model in a simplified manner these subtle effects, thanks to the one-species, one-temperature approach in which one defines a modified electrical conductivity value in the vicinity of the cathode and anode boundaries. In the cathode region, this modified conductivity is taken at the value of the plasma at a $\delta l_{cat} = 0.1$ mm Euclidean distance from the CPI. Similarly, in the anode region, the modified conductivity value is assigned to the value at a $\delta l_{ano} = 0.4$ mm Euclidean distance from the API. Furthermore, one introduces source terms in the energy equation at both the CPI and the API, as presented in section 3.2.2, to account, in a simplified manner, for the electronic heat sources.

3.1.2 Electro-magneto-static equations

The equation used to solve our electrostatic model for the voltage variable ϕ across the entire domain is as seen below, where the electrical conductivity σ^* is a function of temperature:

$$-\nabla\cdot\sigma^*\nabla\phi = 0 \tag{4}$$

The set of equations to solve for the magnetic density flux variable $\boldsymbol{B}$ across the entire domain are:

$$\nabla \wedge \boldsymbol{B} = \mu_0 \boldsymbol{j} \quad ; \quad \boldsymbol{j} = -\sigma^*\nabla\phi \tag{5}$$

$$\nabla\cdot\boldsymbol{B} = 0 \tag{6}$$

where $\mu_0 = 4\pi.10^{-7}\,\mathrm{H}\cdot\mathrm{m}^{-1}$ is the magnetic permeability value in vacuum and $\boldsymbol{j}$ is the current density in $\mathrm{A}\cdot\mathrm{m}^{-2}$. Due to rotational symmetry in our model, only the azimuthal component of $\boldsymbol{B}$ exists.

3.2 Dilatational fluid flow model in the arc-plasma

3.2.1 Mass and momentum equation

The dilatational Navier-Stokes equations are presented below, where the fluid flow is assumed to be in a low Mach number regime [4], so mass density ρ and dynamic viscosity μ vary only with temperature. The set of equations to solve for the unknown velocity $\boldsymbol{u}$ and pressure p fields in Ω_{pla} is:

$$(\boldsymbol{\nabla u})\cdot\rho\boldsymbol{u} = -\nabla p + \boldsymbol{\nabla}\cdot\mu\left(\boldsymbol{\nabla u} + \boldsymbol{\nabla}^t\boldsymbol{u} - \frac{2}{3}(\nabla\cdot\boldsymbol{u})\mathbb{I}\right) + \boldsymbol{f}_{\text{Lor}} \tag{7}$$

$$0 = \rho\nabla\cdot\boldsymbol{u} + \boldsymbol{u}\cdot\nabla\rho \tag{8}$$

where the momentum diffusion term is made up of the shear viscous tensor ($\boldsymbol{\nabla u} + \boldsymbol{\nabla}^t\boldsymbol{u}$) and the dilatational viscous tensor ($-\frac{2}{3}(\nabla\cdot\boldsymbol{u})\mathbb{I}$). The Lorentz force, $\boldsymbol{f}_{\text{Lor}}$, is modelled as a momentum source term:

$$\boldsymbol{f}_{\text{Lor}} = \boldsymbol{j}\wedge\boldsymbol{B} = -\sigma^*\nabla\phi\wedge\boldsymbol{B}$$

Furthermore, it is assumed that buoyancy is negligible in the fluid flow of the plasma, as compared to the Lorentz force and the dilatational effects. Therefore, it is not accounted for in the present model.

3.2.2 Heat transfer equations

The equations to solve for the temperature variable T are as follows:

$$0 = \nabla\cdot\lambda\nabla T + s_{\text{Joule}} \quad \text{in} \quad \Omega_{cat,ano} \tag{9a}$$

$$\rho c_p\boldsymbol{u}\cdot\nabla T = \nabla\cdot\lambda\nabla T + s_{\text{Joule}} - s_{\text{Ray,pla}} \quad \text{in} \quad \Omega_{pla} \tag{9b}$$

where the thermal conductivity λ, the mass density ρ and specific heat capacity c_p are functions of temperature. Equation (9a) models the diffusive heat transfer in the solid cathode and anode domains. On the other hand, equation (9b) models the heat transfer in the arc plasma domain. Furthermore, the volumic source terms are present due to the Joule effect in the entire system along with the emissive volumic radiation term in Ω_{pla}:

$$s_{\text{Joule}} = \sigma^*\nabla\phi\cdot\nabla\phi$$

$$s_{\text{Ray,pla}} = 4\pi\epsilon_n \quad \forall \quad \epsilon_n = f(T)$$

and the plasma emissivity function ϵ_n is plotted in the appendix A.1, in figure 16, j). Due to the thermo-electric phenomena found on the CPI and API, we add the following interfacial conditions:

$$q_{cat} - q_{pla-cat} = s_{\text{Neu}} - s_{\text{Emi}} - s_{\text{Ray,cat}} \quad \text{along} \quad \Gamma_{CPI} \tag{11}$$

$$q_{ano} - q_{pla-ano} = s_{\text{Abs}} - s_{\text{Ray,ano}} \quad \text{along} \quad \Gamma_{API} \tag{12}$$

where $q_{pla-cat}$, $q_{pla-ano}$ are the heat conducted from the plasma to its respective adjacent domain (cathode or anode, respectively); and q_{cat}, q_{ano} the net heat into the respective adjacent domain (cathode, anode), where $q = \boldsymbol{q}\cdot\boldsymbol{n}$. The heat flux $\boldsymbol{q}$ is defined by Fourier's law $\boldsymbol{q} = -\lambda\nabla T$. The source terms at the interfaces are present due to electronic absorption at the API s_{Abs}, Stefan–Boltzmann type radiation s_{Ray}, ionic neutralisation s_{Neu} and thermionic emission s_{Emi} at the CPI:

$$s_{Abs} = j_{API}W_{\text{ano}} \qquad s_{Ray,\Gamma} = \epsilon\sigma_{\text{B}}T_\Gamma^4 \qquad s_{Neu} = j_{\text{Ion}}V_i \qquad s_{Emi} = j_{\text{e}^-}W_{\text{cat}}$$

where σ_{B} is the Stefan-Boltzmann constant: $\sigma_{\text{B}} = 5.6704\times10^{-8}$ $\text{W}\cdot\text{m}^{-2}\cdot\text{K}^{-4}$ and $j_{API} = \sigma^*\nabla\phi\cdot\boldsymbol{n}_{API}$. W_{ano}, ϵ, V_i, W_{cat} are the workpiece work function, emissivity, ionization potential and the cathode effective

work function. Their values are given in table 6 in appendix A.1. The current densities for the energy balance equation at the cathodic sheath are based on the following equations:

$$j_{\mathrm{e^-}} = j_{CPI} - j_{\mathrm{Ion}} \qquad j_{\mathrm{Ion}} = \max(j_{CPI} - j_{\mathrm{RD}}, 0)$$
$$j_{\mathrm{RD}} = A_r T^2 \exp\left(\frac{-W_{\mathrm{eff,cat}}}{k_{\mathrm{B}} T}\right) \qquad j_{CPI} = \sigma^* \frac{\partial \phi}{\partial \boldsymbol{n}_{\text{cat-pla}}}$$

3.3 Boundary conditions

The imposed boundary conditions for the partial differential equations used in this study are presented in table 1, where the boundary conditions are gathered relative to the equations to which they apply. The segments where the boundary conditions are imposed are based on the schematic presented in figure 1. where, the applied

Electric	
$\phi = 0$	[HI]
$-\sigma \nabla \phi \cdot \boldsymbol{n} = 0$	[EA] ∪ [AB] ∪ [BH] ∪ [IC] ∪ [CD] ∪ [DF]
$-\sigma \nabla \phi \cdot \boldsymbol{n} = \boldsymbol{j}_{\mathrm{imp}}$	[EF]
Heat transfer	
$T = 1000\,\mathrm{K}$	[EF] ∪ [FD] ∪ [CI] ∪ [IH]
$-\lambda \nabla T \cdot \boldsymbol{n} = 0$	[EA] ∪ [AB] ∪ [BH] ∪ [DC]
Magnetic	
$\boldsymbol{B} = 0$	[EA] ∪ [AB] ∪ [BH]
Momentum	
$\boldsymbol{u} \cdot \hat{r} = 0$	[AB] ∪ [BC]
$\boldsymbol{u} \cdot \hat{z} = 0$	[BC] ∪ [CD]
$(\boldsymbol{\sigma} \cdot \boldsymbol{n}) \cdot \hat{r} = 0$	[FD] ∪ [CD]
$(\boldsymbol{\sigma} \cdot \boldsymbol{n}) \cdot \hat{z} = 0$	[FD] ∪ [AB]

Table 1: Applied boundary conditions (cf. figure 1).

inlet electric current $\boldsymbol{j}_{\mathrm{imp}}$ at segment [EF] is imposed in the following manner:

$$\int_{[\mathrm{EF}]} \boldsymbol{j}_{\mathrm{imp}} \cdot \boldsymbol{n}\, d\Gamma_{EF} = I_{\mathrm{imp}} \quad \text{with} \quad I_{\mathrm{imp}} = 200\,\mathrm{A} \;\rightarrow\; \boldsymbol{j}_{\mathrm{imp}} = \frac{I_{\mathrm{imp}}}{\Gamma_{EF}} \cdot \boldsymbol{n}$$

and where the electric problem is approached as a fixed current circuit (at 200 A), from which the voltage is calculated. Regarding the thermal boundary conditions, the zero diffusive flux condition is used to apply both a symmetry condition along boundary [EH] and an exit condition along boundary [DC]. The imposed temperature is chosen based on that used by different authors [13, 11]. Finally, the stress tensor $\boldsymbol{\sigma}$ is classically defined as $\boldsymbol{\sigma} = -P\,\mathbb{I} + \mu\left(\boldsymbol{\nabla u} + \boldsymbol{\nabla}^t \boldsymbol{u} - \frac{2}{3}\nabla \cdot \boldsymbol{u}\mathbb{I}\right)$.

3.4 Material properties

The thermophysical and electric properties of the solid tungsten cathode, the argon plasma and the solid copper anode are assumed to depend only on temperature. The thermophysical properties (ρ, μ, λ and c_p) and the electrical one (σ^*) are drawn from Brochard's PhD [4], and reported in appendix A.1 for self-consistency of the present paper.

4 Numerical model

4.1 Finite element approximations

The finite element method discretises in space the steady state, coupled electromagnetic, heat transfer and dilatational fluid flow equations (presented in sections 3.1, 3.2 and 3.3). The weak variational forms of the equations discussed in section 3 are found in the appendix of Brochard's work [4]. Bi-quadratic finite element approximations (9 node Lagrange finite elements) are used for the discretization of the primary field variables of the problem (ϕ, $\boldsymbol{B}$, $\boldsymbol{u}$ and T), meanwhile, piece-wise, discontinuous but bi-linear approximations are used for the pressure field P. Furthermore, all the temperature dependent physical parameters (σ, λ, etc...) were discretized linearly, continous at interfaces, on each of the elements of the mesh. Our discretization schemes are *Ladyzhenskaya-Babuska-Brezzi* stable [20] and the *Streamline Upwind Petrov-Galerkin* method [14] is used for the advective terms found in both the momentum and heat equations. The voltage, temperature and velocity fields are calculated incrementally using the Galerkin method, while the magnetic field is calculated using the Least-Squares Finite Element Method [16] that requires the minimization of a power density per unit charge functional.

4.2 Meshes

Three meshes have been generated for each case, a coarse, intermediate and fine denoted as $\mathcal{M}_1$, $\mathcal{M}_2$ and $\mathcal{M}_3$, respectively (cf. figure 2 that presents $\mathcal{M}_1$ and $\mathcal{M}_2$ of the PNT $\alpha = 15^o$ case). Our unstructured meshes are built with both triangular and quadrilateral elements, having 7 and 9 nodes each, respectively. The high element density zones in the meshes are generated in regions where high gradients are expected, namely close to the cathode tip, symmetry axis and the API. Table 2 shows the number of elements used for each of the three meshes studied in this article. The number of elements of the three meshes are approximately the same, except for the sharpest cathode geometry, the PNT $\alpha = 15^o$ case.

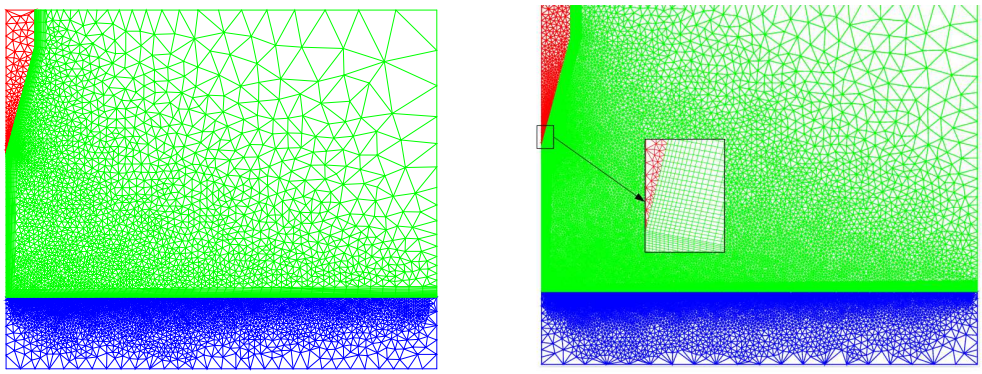

(a) (b)

Figure 2: The meshes for the PNT $\alpha = 15^o$ case. a) $\mathcal{M}_1$: coarsest mesh with $15,487$ elements b) $\mathcal{M}_3$: finest mesh with $42,089$ elements. The red, green and blue zones represent the meshes of the cathode, arc-plasma and anode, respectively.

4.3 Solution strategy

The numerical model involves the non-linear solution between the electromagnetic, heat transfer and fluid flow equations. The non-linearities arise from the advective terms in the energy and momentum equations, radiative losses, temperature dependent physical parameters and electronic source terms at the interfaces. To handle this

	PNT 15^o	PNT $20^o \leq \alpha \leq 30^o$	CHF, all r_{int} $15^o \leq \alpha \leq 30^o$	RND, all r_{int} $15^o \leq \alpha \leq 30^o$
$\mathcal{M}_1$	= 15,487	$\sim$ 4,000	$\sim$ 3,500	$\sim$ 3,500
$\mathcal{M}_2$	= 22,786	$\sim$ 7,000	$\sim$ 7,000	$\sim$ 7,000
$\mathcal{M}_3$	= 42,089	$\sim$ 13,500	$\sim$ 14,000	$\sim$ 14,000

Table 2: The approximate number of elements of the 3 meshes used for all studied cases.

problem numerically, a segregated solution algorithm is used to compute the unknowns incrementally (Newton-like), as depicted in the algorithm schematic (cf. algorithm 1). This algorithm is implemented in the CastɜM modelling toolbox [5] and the linear algebraic systems resulting from the spatial discretisation are solved using the direct solver based on the $LDUt$ factorisation implemented in the CastɜM toolbox [5]. The algorithm is run until the convergence criteria in table 3 are met.

	Global	Energy equation	Momentum equation
Max. number of iterations	$n_{\text{glob}} = 10$ to 500	$n_T = 1$ to 5	$n_{\boldsymbol{u}} = 1$ to 2
Min. increment	Not applicable	$\varepsilon_T = 10^{-2}\,\text{K}$	$\varepsilon_{\boldsymbol{u}} = 10^{-2}\,\text{m}{\cdot}\text{s}^{-1}$
Relaxation factor	Not applicable	$\omega_T = 0.4$ to 1	$\omega_{\boldsymbol{u}} = 0.4$ to 1

Table 3: The non-linear parameters of the algorithm. Refer to algorithm 1 details.

Algorithm 1 Non-linear solution algorithm

Initial conditions
$(\phi, \boldsymbol{B}, \boldsymbol{u}, p, T)^0$; $i_{\text{glob}} = 0$
Non-linear global iteration loop
do
  $i_{\text{glob}} \longleftarrow i_{\text{glob}} + 1$
  Modified electrical conductivity calculation σ^* (section 3.1.1)
  Electrostatic problem
  Calculation of the increment of the electric potential $\delta\phi$
  Updating the electric potential $\phi^{i_{\text{glob}}} = \phi^{i_{\text{glob}}-1} + \delta\phi$
  Magnetostatic problem
  Calculation of the increment of the magnetic field $\delta\boldsymbol{B}$
  Updating the magnetic field $\boldsymbol{B}^{i_{\text{glob}}} = \boldsymbol{B}^{i_{\text{glob}}-1} + \delta\boldsymbol{B}$
  Momentum equations
  $i_{\boldsymbol{u}} = 0$
  do
    $i_{\boldsymbol{u}} \longleftarrow i_{\boldsymbol{u}} + 1$
    Calculation of the pressure-velocity increment $(\delta\boldsymbol{u}, \delta p)$
    Updating with a relaxation factor $(\boldsymbol{u}, p)^{i_{\text{glob}}} = (\boldsymbol{u}, p)^{i_{\text{glob}}-1} + \omega_{\boldsymbol{u}}(\delta\boldsymbol{u}, \delta p)$
  until $i_{\boldsymbol{u}} > n_{\boldsymbol{u}}$ **or** $\|\delta\boldsymbol{u}\| < \varepsilon_{\boldsymbol{u}}$
  Energy equation
  $i_T = 0$
  do
    $i_T \longleftarrow i_T + 1$
    Calculation of the temperature increment δT
    Updating with a relaxation factor $T^{i_{\text{glob}}} = T^{i_{\text{glob}}-1} + \omega_T \delta T$
  until $i_T > n_T$ **or** $\|\delta T\| < \varepsilon_T$
  Global convergence criteria
until $i_{\text{glob}} > n_{\text{glob}}$ **and** $(\left\|T^{i_{\text{glob}}} - T^{i_{\text{glob}}-1}\right\| < \varepsilon_T$ **and** $\left\|\boldsymbol{u}^{i_{\text{glob}}} - \boldsymbol{u}^{i_{\text{glob}}-1}\right\| < \varepsilon_{\boldsymbol{u}})$

5 Results and analysis

In this section the results of the parametric study and their analysis for an arc height of 10 mm and a input electric current of 200 A are presented. First we address the estimation of the numerical spatial error, using equation 13. Then we discuss from a physical point of view, the obtained results (influence of electric intensity on transported quantites, arc pressure and shear, heat flux).

Spatial error estimation

A formal discussion on spatial error is out of the scope of the present study, owing to the use of unstructured meshes [28]. However, we have estimated the spatial discretisation error thanks to 13:

$$\text{relative difference} = \left(1 - \frac{f_{\mathcal{M}_2}}{f_{\mathcal{M}_3}}\right) \cdot 100 \tag{13}$$

that takes into account the field values $f_{\mathcal{M}_2}$ and $f_{\mathcal{M}_3}$ at the mesh nodes of meshes $\mathcal{M}_2$ and $\mathcal{M}_3$, respectively. Starting from $\mathcal{M}_1$, we refined the meshes until the main primal variables of our model (ϕ, T, $\boldsymbol{u}$) dropped their relative difference values to $< 10\%$, reaching $\mathcal{M}_3$. As the velocity field is the most mesh sensitive quantity, it is plotted in figure 3 along the symmetry axis for the various meshes and three different geometric configurations. One can observe a satisfactory convergence of the results when refining the mesh from $\mathcal{M}_1$ to $\mathcal{M}_3$.

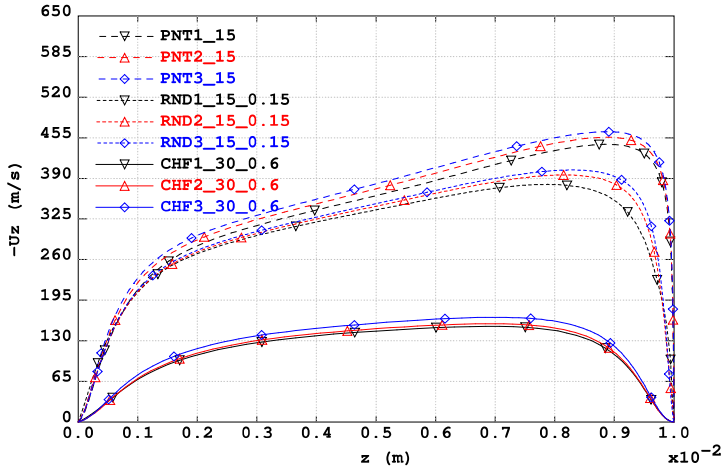

Figure 3: Velocity profiles for the three meshes considered and various cathode shapes. Legend: the first number indicates mesh number, the second one the truncation angle (in degrees) and the third one the tip radius [mm]. The axis origin is at the API.

Physical discussion

In this parametric study aims the magnetic pinching effects induced by the studied geometries of the cathode tip are highlighted. The cathode, arc plasma and the anode are all taken into account in the present model. However, both electrodes are assumed to remain in their solid state. The simplified electric model at the electrode-plasma interfaces allows for a reduction of the computational cost, meanwhile achieving a satisfactory physical representativity. This enables us to account for the geometric effects of the cathode onto the induced electric current density. The arc height of the configuration has been chosen such that the electrical effects at the API become invariant with respect to the studied cathode geometries. Furthermore, to achieve a good trade-off between an acceptable physical representativity and an affordable computational cost, we have used

a purely conductive model in the anode. This aims to model the thermal and electrical sinks in a very cheap way. However this modelling choice infers that any reference to the thermal field in the anode is unrealistic.

5.1 Influence of cathode shape on arc behaviour

The Lorentz force $\boldsymbol{f}_{\mathrm{Lor}}$ is the leading momentum source term in TIG arcs [4, 13, 32], so any modification to this force translates into the behaviour of the arc. The geometry of the cathode tips strongly influences the current density at the CPI, as shown in figure 4, which presents the electric current density $\boldsymbol{j}_{CPI}$ along the curvilinear abscissa at the CPI. The sharper the cathode tip, the more intense the current density profile near the tip, with the maximum current density value rising more than one order of magnitude as compared to the other cases. The different current densities along the CPI result in strongly different Lorentz force fields in the

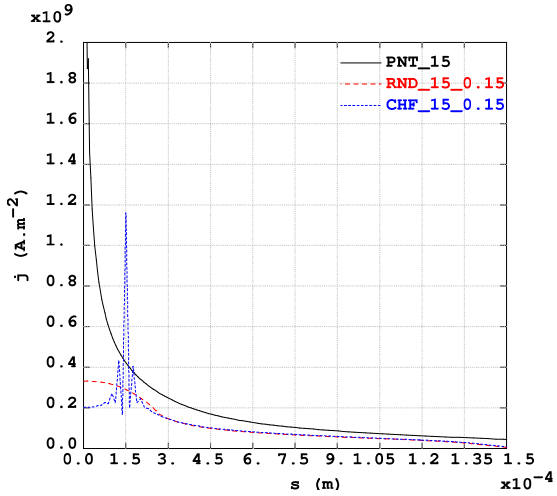

Figure 4: The calculated j_{CPI} for the 3 sharpest cathode cases vs. the curvilinear abscissa along the CPI, where the origin is placed at the tip. The legend lists the geometry type, truncation angle and tip radius, respectively.

arc, as displayed in the top row of figure 5. The computed norm of the Lorentz force is mapped in the vicinity of the cathode tip for the PNT $\alpha = 15^{\mathrm{o}}$ and the RND $\alpha = 20^{\mathrm{o}}$, $r_{int} = 0.6$ mm cases. For the pointed case (cf. figure 5 top left), the Lorentz force is more than one order of magnitude higher than that of the rounded case (cf. figure 5 top right). Furthermore, the volume on which the intense Lorentz force acts on the arc is also much higher for the pointed case. This change in the Lorentz force accordingly influences the velocity field magnitude in the arc-plasma as is seen in the lower row of figure 5. In fact, the magnitude of the velocity field rises 2.8 times from the rounded to the pointed cases presented. This results from the intense magnetic pinching effect of the arc at the sharply pointed tip, which leads to a stronger acceleration of the arc in the direct vicinity of the cathode tip. Therefore, the sharper the cathode tip, the higher the constriction of the arc due to increasing Lorentz forces. These effects translate into higher transported heat flux values and imparted stresses at the anode.

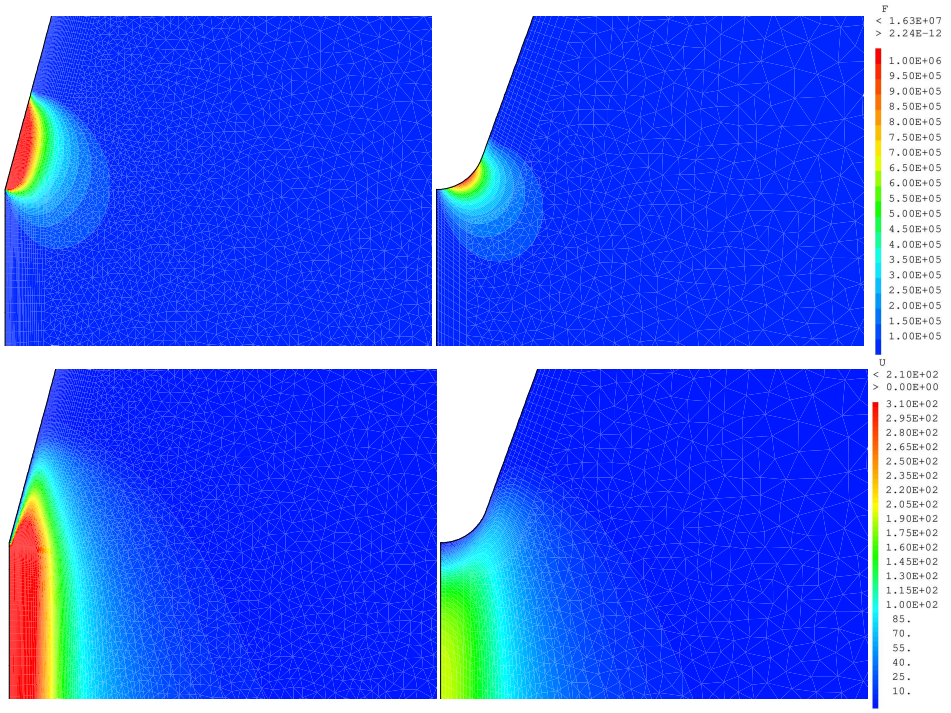

Figure 5: Contour plots of norms of Lorentz force (top row) and velocity field (bottom row) around two different cathode tips. PNT $\alpha = 15^{o}$ (left column) and RND $\alpha = 20^{o}$, $r_{int} = 0.6$ mm (right column) are presented. Lorentz force scale is in [N·m^{-3}] and velocity field in [m·s^{-1}].

We note that the considered pointed cathode configurations are ideal geometries and are physically unrealistic. This is due to geometrical singularities at the tip [15], and this results in temperatures beyond the melting point of tungsten ($T_{melting} = 3680$ K) in its vicinity. This is represented in figure 6 where the temperature profiles at the cathode symmetry axis for the sharpest and bluntest cathodes are plotted. However, although the

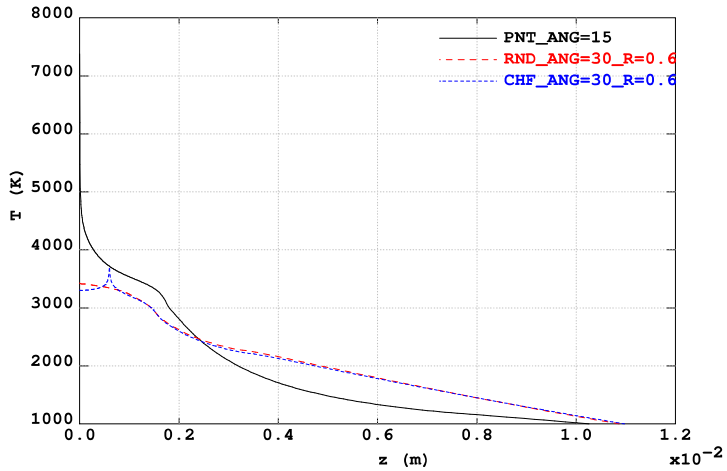

Figure 6: Temperature profiles at the cathode symmetry axis. Graph origin is at the cathode tip.

pointed cathodes are physically unrealistic, they correspond to an extreme geometric limit of cathode shapes. Being the upper limit of cathode sharpness, the pointed cases set the bound on the behaviour of the implemented physical model; while the bluntest chamfered and rounded cases set the lower bound. Thus, studying the physical model at the geometric extremes, the behaviour of the model at any intermediate cathode geometry can be understood.

5.2 Influence of the cathode shape at the plasma-anode interface

To better understand the underlying mechanisms at play in this parametric study, we discuss how the heat flux and mechanical stresses act at the API. Three heat transfer modes make up the total heat transferred to the anode at the API, and they are made up of a diffusion, radiation and an electronic absorption term. Their computed profiles along the radial direction at the API are presented in figure 7.

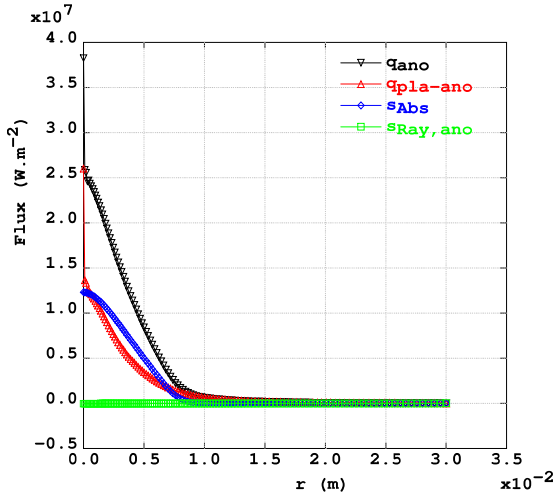

Figure 7: Heat transfer modes at the API for the RND $\alpha = 30^{\circ}$, $r_{int} = 0.6$ mm case. Negative values represent the heat flux leaving the anode, and the positive one, entering it.

Integrating the corresponding fluxes over the API, the radiated heat power is about 65 W while both the heat powers by electronic absorption and the conducted heat from the plasma are of the order of 10^3 W. These trends are found for all studied cases and not just for the presented case. This implies that only the electronic absorption and conducted heat terms play a dominant role in contributing to the heat flow at the API. Therefore, the total heat flow absorbed by the anode is dominated by both the electronic absorption and conducted heat terms. The electronic absorption term, being directly proportional to the electric current density at the API, varies proportionally to the j_{API} profile. Furthermore, because the conducted heat at the API is influenced by the advection of heat in the arc, it increases as the advection in the arc rises. This is due to the large Peclet number in the arc, ($Pe \sim 10^2$) as estimated for the studied cases ($Pe = LU/\alpha_d$, for $L_{arc} = 10$ mm, $U \sim 10^2$ m·s^{-1}, $\alpha_d \sim 10^{-3}$ m^2·s^{-1}). Consequently, a rise in the Peclet number of the arc increases the integrated conducted heat from the plasma to the anode, as is presented in figure 8.

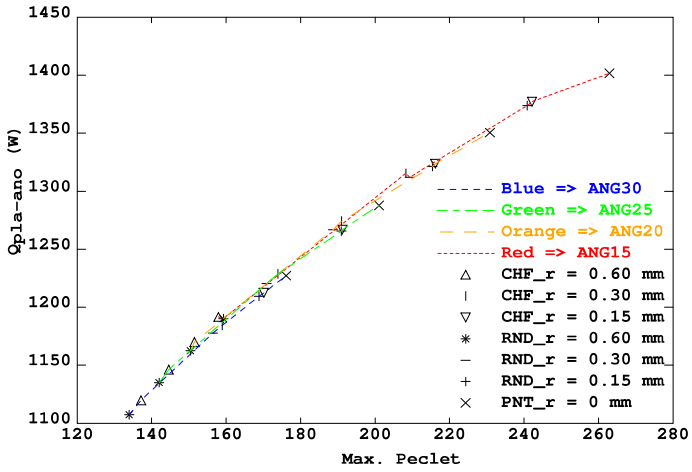

Figure 8: Heat flux transferred to workpiece across the API versus maximum Peclet number in the arc. The color key groups cathodes of same angle, while the marker key groups cathode shape and tip size.

The rise in conducted heat as a function of arc Peclet number is essentially a rise in the transported heat of the arc as a function of cathode tip sharpness.

In the following subsection, we have quantified the influence of the cathode geometry on to the physical quantities of interest at the API (arc pressure, arc shear stress and the total heat flux to the anode).

5.2.1 Transported quantities at the plasma-anode interface

The impact of the variability in the Lorentz forcing of the flow is directly seen in the arc velocity profiles, where the velocity fields get stronger as the cathode tips get sharper. The direct influence of cathode sharpness on arc velocity is presented in figure 9, where the maximum arc velocities are plotted as functions of truncation angle and tip size. This significant rise in maximum arc velocity with tip sharpness significantly influences the pressure, shear and heat flux profiles of the arc at the API.

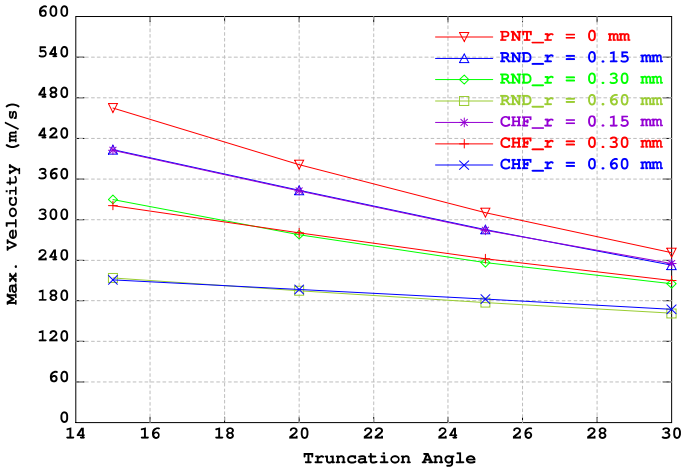

Figure 9: Maximum arc velocity versus truncation angle (in degrees) and tip type.

To quantify the variability in the stresses and heat flux profiles at the API, two analytical functions are used to simplify the discussion. The functions are fit to the profiles of interest at the API similarly to Alvarez et al. [8]. However, we use simpler (less parameters) analytical fits, motivated by the work in [18, 19, 26]. The heat

flux q_{ano} and the pressure P at the API are fitted with the following Gaussian distribution:

$$g(r) = g_{max} \exp\left(\frac{-r^2}{2{\sigma_g}^2}\right) \tag{14}$$

The shear stress τ at the API is fitted with a scaled Weibull distribution as follows:

$$w(r) = w_{max}\left[\frac{r}{\lambda_w}\left(\frac{k}{k-1}\right)^{\frac{1}{k}}\right]^{k-1} \exp\left[\frac{k-1}{k} - \left(\frac{r}{\lambda_w}\right)^k\right] \tag{15}$$

The functions are fit by centering them at the maximum values of the profiles $q_{max}, P_{max}, \tau_{max}$ and by constraining the integrals of the fitting functions to the integral heat and force values. The widths of the numerical profiles are quantified using the variance σ_g of equation 14 and the scale λ_w of equation 15. The shape parameter k of equation 15 dictates the shape of the Weibull distribution.

The variability in the magnetic pinching effect as a function of tip sharpness translates to significant variability in the transported arc quantities at the API. Between the bluntest and the sharpest cathodes, the maximum pressure P_{max} and shear stress τ_{max} at the API increases ≈ 3.5 and ≈ 4-fold, respectively, while the maximum heat flux q_{max} increases ≈ 1.7-fold. Moreover, as the maxima rise with respect to tip sharpness, the widths of the pressure, shear and heat flux profiles consequently drop. The widths σ_P, λ_τ of the pressure and shear profiles at the API drop ≈ 1.6-fold, while the widths σ_q of the heat flux profiles drop ≈ 1.3-fold between the bluntest and sharpest cathode tip. As the stress profiles intensify with cathode tip sharpness, the total imparted integrated pressure and shear forces increase ≈ 1.5-fold and ≈ 1.8-fold respectively. The total heat flux into the anode increases ≈ 1.2-fold. These trends are visualized in figure 10. The numerical profiles and the fitted functions to the normalized pressure, shear stress and heat flux variables are presented for the PNT $\alpha = 15^o$ and the CHF $\alpha = 30^o$ $r_{int} = 0.6$ mm cases in figures 10 a), b) and c), respectively. The integrated pressure and shear forces are plotted in figures 10 d), e) and the integrated heat flux into the anode in f). The maxima and the fitted widths of the pressure, shear and heat flux values of all the simulated cases in this study are presented in figure 11. Figures 11 a) and b) present the maxima and Gaussian variance of the fitted pressure profiles; figures 11 c) and d) the maxima and Weibullian scale of the fitted shear profiles; figures 11 e) and f) the maxima and Gaussian variance of the fitted heat flux profiles respectively, of all simulated cases in this study. The shape parameter k is approximately constant for all Weibull distributions fitted to the shear profiles, with $k \approx 1.4$.

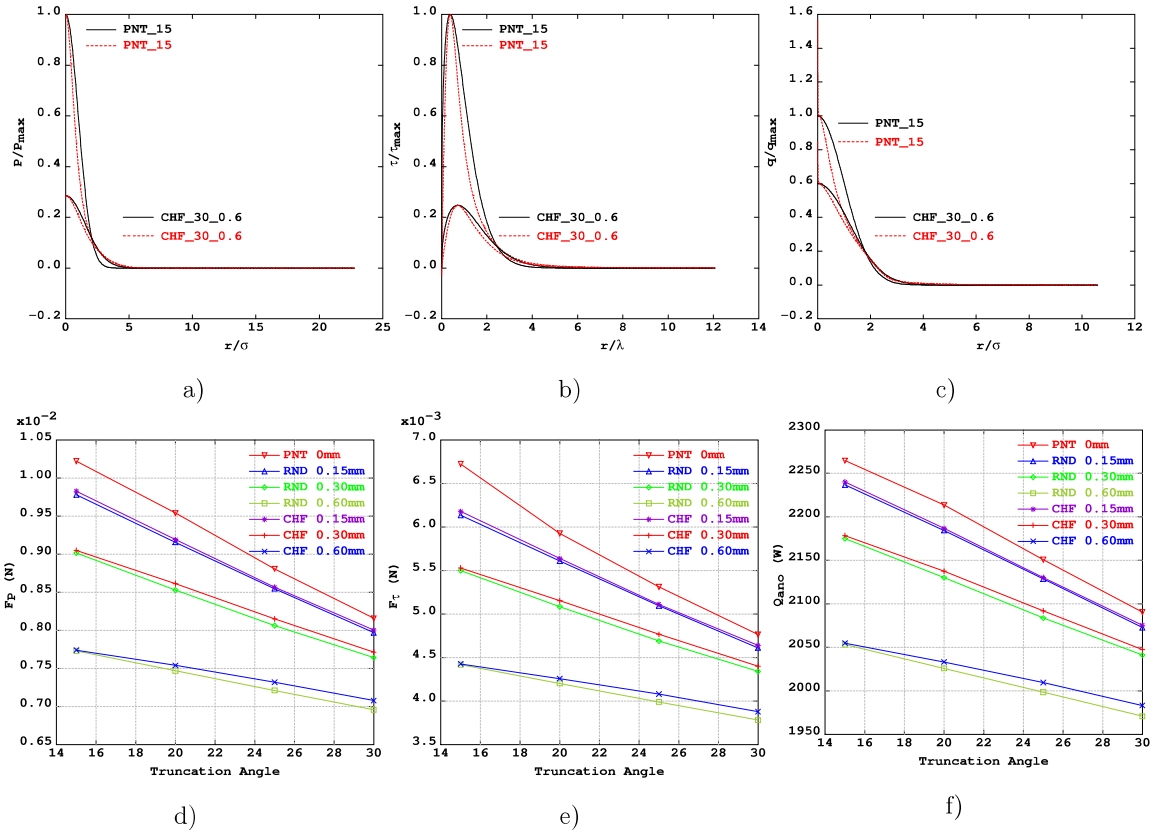

Figure 10: a) Normalized Gaussian fits and pressure profiles; b) normalized Weibull and shear stress profiles; c) normalized Gaussian fits and heat flux profiles for PNT $\alpha = 15^{\text{o}}$ and CHF $\alpha = 30^{\text{o}}$, $r_{int} = 0.6$ mm cases. Black solid lines and red dashed lines indicate the fits calculated profiles, respectively. Axes are non-dimensionalized w.r.t PNT $\alpha = 15^{\text{o}}$ case. d) The integrated pressure force; e) the integrated viscous shear force; f) the integrated heat flux versus cathode geometry.

The variability of the electric current density profile j_{API} at the API is calculated to be weak for a 10 mm arc. The j_{API} profiles across different cases is negligible where the maximum current densitiy j_{max} and the fitted Gaussian widths σ_j are seen below:

$$2.85 \times 10^6 \quad \leq \quad j_{max} \leq 3.11 \times 10^6 \quad [\text{A} \cdot \text{m}^{-2}] \tag{16}$$

$$3.20 \quad \leq \quad \sigma_j \quad \leq \quad 3.34 \quad [\text{mm}] \tag{17}$$

The sharper the geometry of the cathode tip, the more energy and momentum is transported by the arc from the cathode to the anode. These trends are captured by our model because the cathode is included in the calculation domain. Thus the geometry of a cathode requires attention when setting up a TIG welding configuration for simulation.

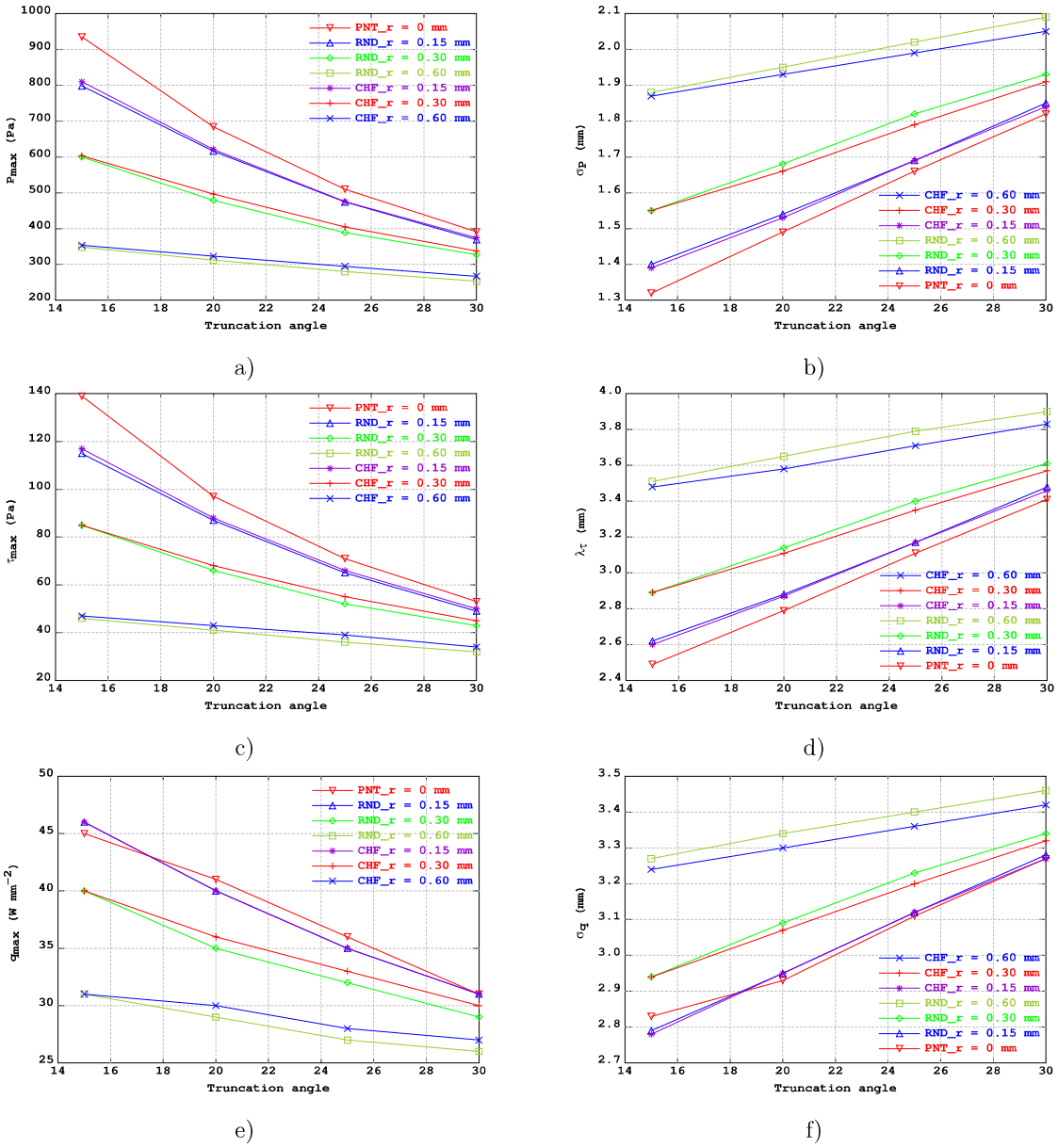

Figure 11: a) Maxima of pressure profiles; b) Gaussian variances of fitted pressure profiles; c) maxima of shear profiles; d) Weibull scales of fitted shear profiles; e) maxima of heat flux profiles; f) Gaussian variances of fitted heat flux profiles versus truncation angle (degrees) and tip type.

5.2.2 Analysis of the results

This study assumes a solid anode so as to isolate the effects of cathode tip geometry onto TIG arcs. The use of a solid anode maintains a constant arc height unlike in actual welding conditions which leads to a deformable melt pool in the anode domain [26]. By solely increasing the sharpness of a cathode tip, the momentum and heat transported by a TIG arc increases. Referring to the figures 10 and 11 we note that the maximum stresses and the heat fluxes at the API increase roughly 4 and 1.7 times, respectively, from the bluntest to the sharpest cathode tips. This variability is significant and important to capture in TIG welding simulations, as is already reported in the literature on experimental observations [17, 31, 24, 29, 35]. Therefore, when setting up numerical simulations, one should pay attention when accounting for cathode shape in the model. Indeed, it appears that in some early numerical studies the sensitivity of the momentum and mass equations to the magnetic pinching

effect is overlooked [13, 11, 3]. With the Lorentz force being the main source of momentum in the arc-plasma, any variation in this force translates into a variation in the velocity field, as is presented in figure 9. Furthermore, the variability of the Lorentz force is directly due to its sensitivity to the electric current density in the vicinity of the cathode tip. From figure 4, we note the sensitivity of the electric current density to the geometry at the cathode tip. This sensitivity is captured by the explicit inclusion of the cathode into the calculation domain. The sensitivity is due to the $\nabla\phi|_{\Gamma_{CPI}}$ term that increases in intensity as the tip geometry gets sharper [9, 15].

For the considered arc-plasma of a 10 mm height and 200 A inlet current, the calculated variability in the heat flux transported to the API is dictated by the variability in the conducted heat term $q_{pla-ano}$. This is because the variability in the electronic absorption term s_{Abs} at the API is negligible due to the arc becoming relatively insensitive to the voltage field near the anode. This insensitivity implies that the electric current density once it reaches the API becomes roughly constant, as shown in the inequalities (16) and (17). The calculated conducted heat flux $q_{pla-ano}$ varies with the sharpness of the cathode tip due to its dependence on the advected heat of the arc. Referring to figure 8, it turns out that the transferred heat flux to the anode depends on the Peclet in a quasi-linear way. Therefore, the magnitude of the arc velocity, which depends on the Lorentz force and consequently on the cathode geometry, strongly influences the heat flux at the API.

Although variability is calculated in the transported quantities across most studied cases, negligible variation is seen between simulations of the CHF and RND type; as is observed in figures 8, 9, 10, 11, where their results overlap. However, although the electric current density locally differs between the CHF and RND (cf. figure 4) this localized difference does not dominate the entirety of the profile, and only makes up a couple of Amperes in electric current. Therefore, the Lorentz force resulting from the CHF and RND cases are very similar, cf. figure 12, which presents the contour plots of the Lorentz force in the vicinity of the RND and CHF cases at $r_{int} = 0.3$ mm, $\alpha = 15^{o}$.

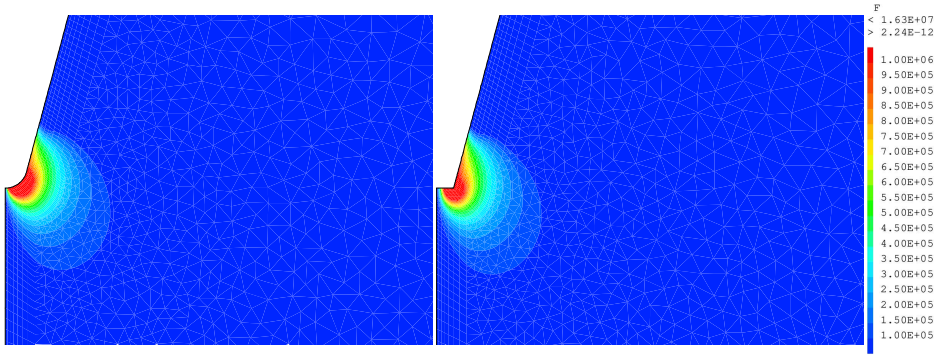

Figure 12: Contour plots of the norms of the Lorentz force around two different cathode tips. The RND (right) and CHF (left) $\alpha = 15^{o}$, $r_{int} = 0.3$ mm cases are presented. The scale is in [N·m^{-3}].

Furthermore, similar results are calculated for multiple cases at different truncation angles and radii. This is observed in figures 8, 9, 10, 11. This weak variability between the cases is attributed to a quasi-equivalence in the total power of the Lorentz force to drive flow in the arc-plasma. The total power is defined by:

$$\mathcal{P} = \int_{\Omega_{pla}} \boldsymbol{u} \cdot \boldsymbol{f}_{Lor} \, d\Omega \tag{18}$$

where $\mathcal{P}$ [W] represents the total power in driving the fluid flow. The power of the Lorentz force for all simulated arcs in this study is presented in figure 13. Referring to the figure, the cases with quasi-equivalent power values are encased by a specific black marker (circular, triangular and rectangular markers). Provided that the integral power of the Lorentz force is similar, the resulting transported quantities at the API will also be comparable, irrespective of the cathode shape.

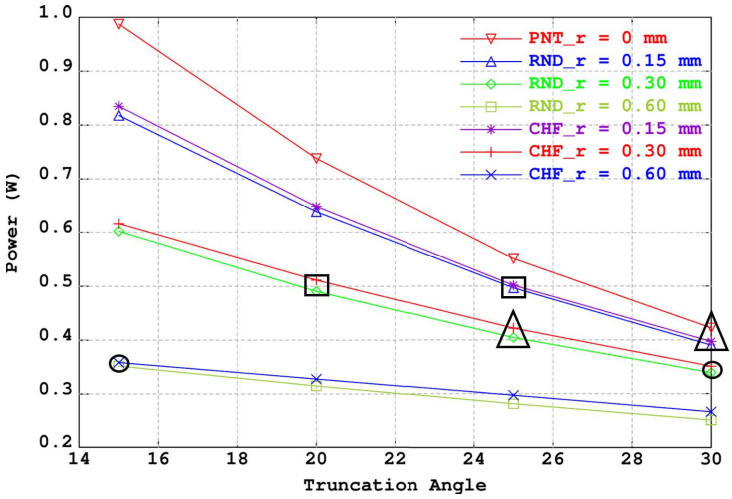

Figure 13: Mechanical power of the Lorentz force in the arc versus cathode geometry. Each black shape groups cases that have quasi-equivalent power values.

5.2.3 Voltage drop and arc efficiency

The voltage drop across the TIG circuit is calculated by imposing a constant current at the input boundary of the cathode. Figure 14 presents the voltage drop across the entire domain versus cathode geometry.

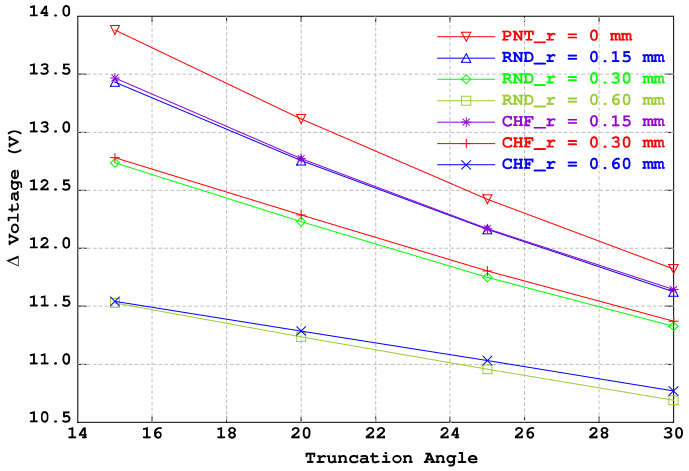

Figure 14: The voltage drop versus the different cathode geometries.

The voltage drop increases w.r.t increasing tip sharpness. This proportionally increases the total energy available in the circuit as $\mathcal{P}_{circuit} = I\Delta\phi$ [W], with $\Delta\phi$ the voltage drop, and I the input current at a constant 200 A. The voltage drop as a function of α and r_{int} is presented in figure 14. The more the electric power is pulled by the circuit, the more the heat is deposited at the anode. Correspondingly, figure 10 (d) shows that the sharper the cathode tips, the larger Q_{ano} is at the work piece. The ratio of the rise of energy deposited by the arc and power pulled into the circuit is quantified by calculating the efficiency η of the circuit. The equation used to calculate the circuit efficiency takes into account the source and sink terms injected at the interfaces at both the CPI and API is:

$$\eta = \frac{Q_{ano}}{P_{circuit} + \int \left[s_{Abs} - s_{Emi} + s_{Neu} \right] d\Gamma} \times 100\% \tag{19}$$

see section 3.2.2 for details about the source and sink terms. Although the thermal and dynamic performance of the arc w.r.t truncation angle and tip radius displays variation, the arc efficiency is largely independent of

the cathode shapes studied in this work. A maximum difference of $\approx 3\%$ is calculated across all cases, for $65\% \leq \eta \leq 68\%$. This is due to a good positive linear correlation between Q_{ano} and $P_{circuit}$ w.r.t tip sharpness.

5.3 A discussion with respect to similar works

In this section the results of the present study are compared to those found in the literature on both numerical and experimental works.

5.3.1 Comparison to simulations

The first comparison is performed with a numerical study from Goodarzi et al. [11], in which a wide range of truncation angles[1], ranging from $4.59^{o} \leq \alpha \leq 75^{o}$, were considered. Instead of incorporating the cathode into their calculation domain, they imposed an electric current density at the cathode tip as a boundary condition. The electric current density is imposed using spot areas experimentally estimated by Haidar et al. [12]. Figure 15 a) sketches the electric current density distribution as imposed at the cathode tip in Goodarzi's work, and the one resulting from the computation from the present model.

The magnitudes of the main variables of the TIG arc system are presented in table 4 for both the Goodarzi et al. study [11] and ours. Comparing the maximum heat flux pulled into the anode between the bluntest and sharpest cases, Goodarzi et al. calculated negligible variation ($\approx 0.15\%$), whereas our calculations reveal a ≈ 1.7-fold increase. Moreover, referring to the maximum arc velocities, pressures and shear stresses, the values calculated by Goodarzi et al. vary significantly less than ours. Furthermore, we note that the electric current density, at the cathode tip, is quasi-constant for the range of cases studied by Goodarzi et al.. Indeed, as previously stated, the electric current density in the vicinity of the cathode tip directly influences the Lorentz force. Therefore, a lack of variability in the electric current density translates into negligible differences in the transported quantities of the arc. For ease of comparison and due to the fact that the spot size is the critical boundary condition in Goodarzi's work [11], the cathode spot area sizes of our study are estimated. We define the spot size as the zone where 150 A of current passes through our cathode. Our estimated spot areas are presented in figure 15 figure (b), along with those from Goodarzi [11] and Haidar [12]. The variability of the spot sizes w.r.t truncation angle, tip radius and shape shows a ≈ 3 fold maximum variation in area size. Moreover, our estimated spot areas do not exceed 2.4-times the values used by Goodarzi et al.. Thus, the variability calculated in our estimated spot areas is not sufficient to explain the ≈ 1000-fold (see table 4) ratio that we obtained in the electric current densities between the bluntest and sharpest cathode tips. Therefore, we deduce that the spot area boundary condition method used by Goodarzi et al. is not adapted for the capturing of the variation of electric current density at the tip. Indeed, the spot areas are incapable of capturing the local behavior at the cathode tip, because the spot is interpretable as an integral quantity; masking any local $\boldsymbol{j}$ gradients that can influence the Lorentz force of the arc flow. Thus, the spot area boundary condition method is not adapted to capturing the influence of tip sharpness onto TIG arcs. Furthermore, the necessity to account for the cathode geometry in the computational domain when modelling TIG arcs is highlighted.

[1] They assign values to the cone angle, whereas in the present work, the half angle is used.

Variable	$j_{CPI,max}$ [A·mm^{-2}]			q_{max} [W·mm^{-2}]			u_{max} [m·s^{-1}]		
Case	Bluntest	Sharpest	Ratio	Bluntest	Sharpest	Ratio	Bluntest	Sharpest	Ratio
Goodarzi [11]	≈ 200	≈ 200	1	39.30	39.84	1	398.9	413.8	1.04
This work	40	30000	750	27	45	1.7	170	470	2.8

Variable	P_{max} [Pa]			τ_{max} [Pa]		
Case	Bluntest	Sharpest	Ratio	Bluntest	Sharpest	Ratio
Goodarzi [11]	850	1078	1.3	125	150	1.2
This work	267	935	3.5	34	139	4

Table 4: Characteristic results from Goodarzi et al. [11] and from the present study.

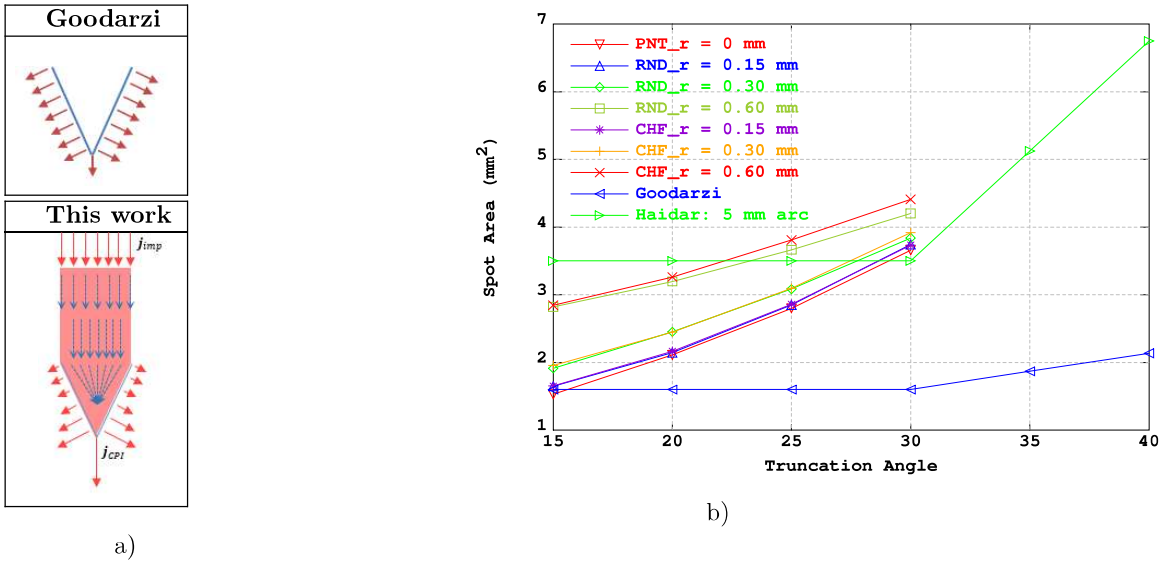

Figure 15: a) Schematic representations of electric current emission zone for Goodarzi's cathode, and ours. b) Estimated spot areas in this study, those used in Goodarzi [11] and those from Haidar [12] versus cathode geometry. The error bars from Haidar's work are not displayed.

5.3.2 Comparison to experiments

In this subsection, we compare our calculated results to several experimental studies that deal with the influence of cathode tip sharpness on to TIG arcs. Mills et al. [24] note the 4-fold increase in maximum arc pressure as the cathode tip truncation radius decreases to $r_{int} = 0$ for a constant tip truncation angle of $\alpha = 15^o$. Furthermore, the maximum arc shear stress rises similarly with the arc pressure for typical TIG arcs. Tsai [35] observes that the maximum heat flux transported to the anode increases 1.2-fold as the truncation angle is sharpened from $\alpha = 30^o$ to $\alpha = 15^o$. Petrie et al. [36] observe for a 10 mm and 200 A arc, that the maximum arc velocity dropped 2-fold between their sharpest and bluntest cathodes. Consequently they note a $\approx$ 3.5-fold drop in the measured maximum arc pressure. They claim a 1.3-fold drop in the conducted heat flux as their cathode tip sharpness drops. Sadek et al. [29] observe a $\approx$ 4.5-fold rise in the maximum arc pressure as the cathode tip radius tends to $r_{int} = 0$ mm. Concerning the total drop voltage, we performed a brief comparison with the experimental results from Chihoski [6], for which two of his studied trunctation angles correspond to ours ($\alpha = 15^o$ and 30^o). We have reported the total drop voltage as it is calculated explicitly using our one-species, one-temperature model (This work a)) along with the corrected value that accounts for the voltage drops across the CPI and API (This work b)), according to the method used by Tanaka et al. [32]. The general trends are well reproduced by our model, with an agreement from 0.5% up to 7%, for the bluntest to sharpest cases, respectively. Nevertheless, the experimental setups used by the cited authors do not exactly correspond to the

configuration used in our numerical study (different arc heights and tip truncation radii). To better validate our numerical model, supplementary experimental studies are recommended. The discussed results borrowed from the literature are summarized in table 5 and compared to the trends calculated in this work. From the

Variable	Max. pressure [Pa]			Max. shear [Pa]			Max. heat flux [W·mm^{-2}]		
Case	Bluntest	Sharpest	Ratio	Bluntest	Sharpest	Ratio	Bluntest	Sharpest	Ratio
Mills [24]	≈ 390	≈ 1470	≈ 4	——	——	≈ 4	——	——	——
Tsai [35]	——	——	——	——	——	——	≈ 27	≈ 32	≈ 1.2
Petrie [36]	≈ 400	≈ 1400	≈ 3.5	——	——	——	——	——	1.3
Sadek [29]	≈ 500	≈ 2200	≈ 4.5	——	——	——	——	——	——
This work	267	935	3.5	34	139	4	27	45	1.7

Variable	$\Delta\phi$ [V]		
Case	Bluntest	Sharpest	Ratio
Chihoski [6]	17.9	18.6	1.041
This work a)	11	13	1.18
This work b)	18	20	1.11

Table 5: Results from experimental studies in the literature versus this study.

quantitative comparison presented in table 5 it turns out that the present model is capable of reproducing the general experimental trends concerning the main physical quantities of interest. Moreover, it is interesting to note that Tanaka et al. [33] observe, for arc configurations similar to ours, that the electric current density at the API does not significantly vary with cathode tip geometry. Thus, we consider that the model implemented in this study is relevant to capturing the effects of cathode tip geometries on TIG arcs.

6 Conclusion

This paper presents a numerical parametric study, that aims at showing the influence of the cathode tip geometry onto the relevant welding quantities, such as the heat transferred to the anode, the arc pressure and shear stress at the workpiece. The model implemented in the present work accounts for both the cathode, arc and anode subdomains in the computational domain. However, the electrodes are assumed to remain solid and to behave in a purely diffusive manner. A TIG Spot configuration being considered results in rotational symmetry, that leads to 2D axi-symmetric computations. The studied configurations consider a 10 mm arc height, a 200 A inlet electric current, for three tip shapes: pointed, chamfered and rounded tips. The range of truncation angles and radii are: $\alpha = [15^o\ ,\ 20^o\ ,\ 25^o\ ,\ 30^o]$; and $r_{int} = [0.15\ ,\ 0.3\ ,\ 0.6,]$ mm.

The main findings of this work are three-fold. First, the shape of the cathode tip strongly influences the current density at the cathode-plasma interface, that in turn significantly affects the resulting Lorentz force. This being the main source of momentum in the fluid flow of the arc-plasma, it induces a broad variability of the transported quantities relevant to the welding parameters. Indeed the heat flux pulled in by the anode shows a direct dependence on the Peclet number, which reflects the magnitude of the fluid flow in the arc-plasma. The heat flux varies up to 1.7 times, while the pressure and shear stresses rise about 4 times, respectively, from the bluntest to the sharpest tips. Therefore, this parametric study strongly suggests the importance of considering the cathodes in the computational domain, in order to reliably account for the magnetic pinching induced by the tip of the cathode. On the other hand, the considered pointed cathode configurations are ideal geometries that can not exist in the real world. They lead to a geometrical singularity at the tip, that results in spurious computations in its vicinity, that overestimates the physical quantities. However, they enable to capture the trends up to the limiting case. Finally, the general agreement between our results and the discussed experimental observations reinforces the validity of our numerical results, and confirms the need to incorporate the cathode into the calculation domain. The authors are aware of the numerous physical limitations of the

present model (TIG Spot, conductive anode, constant arc height and inlet current etc...); however, this work highlights the effect of cathode geometry onto the physical quantities relevant to welding configurations.

A Appendix

A.1 Material properties

Parameter	Symbol	Value	Unit
Tungsten			
Emissivity	ϵ	0.4	–
Work potential	W_{cat}	4.52	V
Effective work potential (Thoriated Tungsten)	$W_{\text{eff,cat}}$	2.63	V
Richardson constant	A_r	3.10^4	$\text{W}\cdot\text{m}^{-2}\cdot\text{K}^{-2}$
Melting Temperature		3680	K
Argon			
Ionization potential	V_i	15.68	V
Copper			
Emissivity	ϵ	0.4	–
Work function	W_{ano}	4.65	V
Melting temperature		1358	K

Table 6: Material properties for Tungsten, Argon and Copper. Assembled in Brochard's work [4]

.

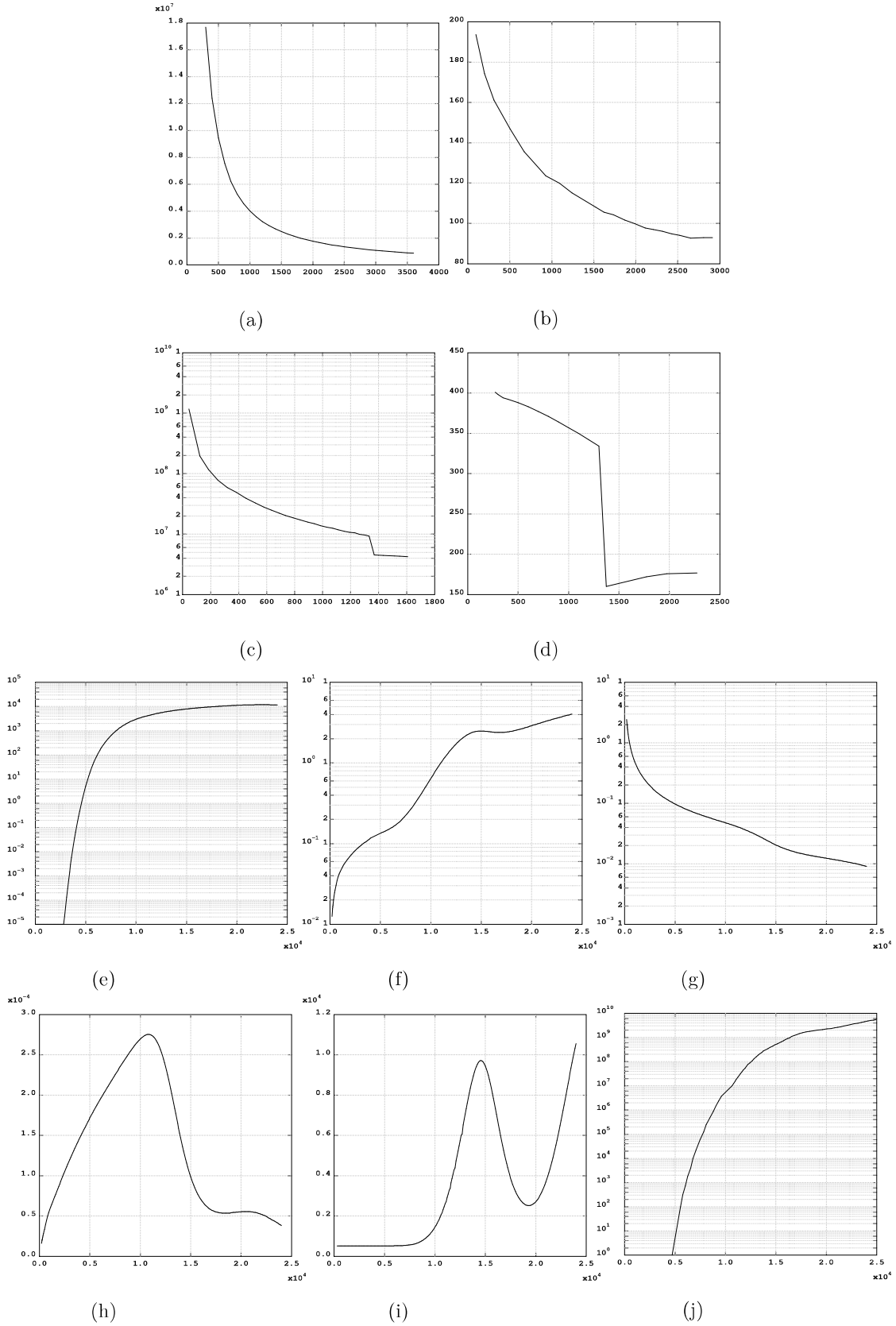

Figure 16: Material properties as functions of temperature T [K]. Subfigures (a) and (b) tungsten, (c) and (d) copper, (e) and (f) argon, present the respective electrical σ [S·m^{-1}] and thermal λ [W·m^{-1}K^{-1}] conductivities of each respective material. Subfigure (g), (h), (i) and (j) present argon density ρ [Kg·m^{-3}], dynamic viscosity μ [kg·m^{-1}s^{-1}], heat capacity c_p [J·Kg^{-1}K^{-1}] and the net plasma emission coefficient ϵ_n [W·m^{-3}sr^{-1}]

Acknowledgements

The first author would like to thank Dr. Anais Baumard for the many fruitful discussions and her help in discussing the results.

References

[1] A. Anders. *Cathodic arcs: from fractal spots to energetic condensation*, volume 50. Springer Science & Business Media, 2009.

[2] T. L. Bergman, F. P. Incropera, D. P. DeWitt, and A. S. Lavine. *Fundamentals of heat and mass transfer*. John Wiley & Sons, 2011.

[3] R. Bini, M. Monno, and M. Boulos. Numerical and experimental study of transferred arcs in argon. *Journal of Physics D: Applied Physics*, 39(15):3253, 2006.

[4] M. Brochard. *Modèle couplé cathode-plasma-pièce en vue de la simulation du procédé de soudage à l'arc TIG*. PhD thesis, Université de Provence (Aix-Marseille I), janvier 2009.

[5] Cast3m. Cast3m Web site. `http://www-cast3m.cea.fr/`.

[6] R. A. Chihoski. The rationing of power between the gas tungsten arc and electrode. *Welding Journal*, 49 (2):69–82, February 1970.

[7] L. P. Connor and R. O'Brien. *Welding handbook: welding processes*, volume 2. American Welding Society, 1991.

[8] A. Delgado-Álvarez, P. F. Mendez, and M. A. Ramírez-Argáez. Dimensionless representation of the column characteristics and weld pool interactions for a DC argon arc. *Science and Technology of Welding and Joining*, pages 1–10, 2019.

[9] G. J. F. G. Strang. An analysis of the finite element method, 1988.

[10] A. Gleizes, J.-J. Gonzalez, and P. Freton. Thermal plasma modelling. *Journal of Physics D: Applied Physics*, 38(9):R153, 2005.

[11] M. Goodarzi, R. Choo, and J. M. Toguri. The effect of the cathode tip angle on the GTAW arc and weld pool: I. mathematical model of the arc. *Journal of Physics D: Applied Physics*, 30(19):2744, 1997.

[12] J. Haidar and A. Farmer. Large effect of cathode shape on plasma temperature in high-current free-burning arcs. *Journal of Physics D: Applied Physics*, 27(3):555, 1994.

[13] K. Hsu, K. Etemadi, and E. Pfender. Study of the free-burning high-intensity argon arc. *J. Appl. Phys.*, 54(3):1293–1301, March 1983.

[14] T. J. Hughes, L. P. Franca, and M. Mallet. A new finite element formulation for computational fluid dynamics: Vi. convergence analysis of the generalized supg formulation for linear time-dependent multidimensional advective-diffusive systems. *Computer Methods in Applied Mechanics and Engineering*, 63(1): 97–112, 1987.

[15] J. D. Jackson. Classical electrodynamics, 1999.

[16] B.-n. Jiang. *The least-squares finite element method: theory and applications in computational fluid dynamics and electromagnetics*. Springer Science & Business Media, 1998.

[17] J. Key. Anode/cathode geometry and shielding gas interrelationships in gtaw. *Weld J.*, 59(12):364, 1980.

[18] C.-H. Kim, W. Zhang, and T. DebRoy. Modeling of temperature field and solidified surface profile during gas–metal arc fillet welding. *Journal of Applied Physics*, 94(4):2667–2679, 2003.

[19] S. H. Ko, C. D. Yoo, D. F. Farson, and S. K. Choi. Mathematical modeling of the dynamic behavior of gas tungsten arc weld pools. *Metallurgical and Materials Transactions B*, 31(6):1465–1473, 2000.

[20] D. Kuzmin and J. Hämäläinen. Finite element methods for computational fluid dynamics: a practical guide. *SIAM Rev*, 57(4):642, 2015.

[21] F. Lago, J. Gonzalez, P. Freton, and A. Gleizes. A numerical modelling of an electric arc and its interaction with the anode: Part I. the two-dimensional model. *Journal of Physics D: Applied Physics*, 37(6):883, 2004.

[22] J. Lowke and M. Tanaka. LTE diffusion approximation for arc calculations. *Journal of Physics D : Applied Physics*, 39:3634–3643, 2006.

[23] F. Matsuda, M. Ushio, and T. Kumagai. Study on gas-tungsten-arc electrode (report 1): Comparative study of characteristics of oxide-tungsten cathode (welding physics, process & instrument). *Transactions of JWRI*, 15(1):13–19, 1986.

[24] K. Mills and B. Keene. Factors affecting variable weld penetration. *International Materials Reviews*, 35 (1):185–216, 1990.

[25] A. B. Murphy. A perspective on arc welding research: the importance of the arc, unresolved questions and future directions. *Plasma Chemistry and Plasma Processing*, 35(3):471–489, 2015.

[26] M. C. Nguyen, M. Medale, O. Asserin, S. Gounand, and P. Gilles. Sensitivity to welding positions and parameters in GTA welding with a 3D multiphysics numerical model. *Numerical Heat Transfer, Part A: Applications*, 71(3):233–249, 2017.

[27] R. Niles and C. Jackson. Weld thermal efficiency of the GTAW process. *Welding journal*, 54(1):25, 1975.

[28] C. J. Roy. Grid convergence error analysis for mixed-order numerical schemes. *AIAA journal*, 41(4): 595–604, 2003.

[29] A. A. Sadek, M. Ushio, and F. Matsuda. Gas-tungsten-arc cathode and related phenomena. *Transactions of JWRI*, 16(1):195–210, 1987.

[30] L. Sansonnens, J. Haidar, and J. Lowke. Prediction of properties of free burning arcs including effects of ambipolar diffusion. *Journal of Physics D: Applied Physics*, 33(2):148, 2000.

[31] W. Savage, S. Strunck, and Y. Ishikawa. The effect of electrode geometry in gas tungsten- arc welding. *Welding Journal*, 44(11):489, 1965.

[32] M. Tanaka, H. Terasaki, M. Ushio, and J. J. Lowke. A unified numerical modeling of stationary tungsten-inert-gas welding process. *Metallurgical and Materials Transactions A*, 33(7):2043–2052, 2002.

[33] M. Tanaka, H. Terasaki, H. Fujii, M. Ushio, R. Narita, and K. Kobayashi. Anode heat transfer in tig welding and its effect on the cross-sectional area of weld penetration. *Welding international*, 20(4):268–274, 2006.

[34] A. Traidia. *Multiphysics modelling and numerical simulation of GTA weld pools*. PhD thesis, 2011.

[35] N. Tsai. *Heat distribution and weld bead geometry in arc welding*. PhD thesis, Massachusetts Institute of Technology, 1983.

[36] E. P. T.W Petrie. The influence of the cathode tip on temperature and velocity fields in a gas-tungsten arc. *Weld Research and supplement*, 1970.